Applied Physics Letters ARTICLE scitation.org/journal/apl

Structural and piezoelectric properties of ultra-thin $Sc_xAl_{1-x}N$ films grown on GaN by molecular beam epitaxy

Cite as: Appl. Phys. Lett. **117**, 112101 (2020); doi: 10.1063/5.0013943
Submitted: 17 May 2020 · Accepted: 28 August 2020 ·
Published Online: 14 September 2020

View Online

Export Citation

CrossMark

Joseph Casamento,[1,a)] Celesta S. Chang,[2,3] Yu-Tsun Shao,[3] John Wright,[1] David A. Muller,[3,4] Huili (Grace) Xing,[1,4,5] and Debdeep Jena[1,4,5]

AFFILIATIONS

[1]Department of Materials Science and Engineering, Cornell University, Ithaca, New York 14853, USA
[2]Department of Physics, Cornell University, Ithaca, New York 14853, USA
[3]School of Applied and Engineering Physics, Cornell University, Ithaca, New York 14853, USA
[4]Kavli Institute at Cornell for Nanoscale Science, Cornell University, Ithaca, New York 14853, USA
[5]School of Electrical and Computer Engineering, Cornell University, Ithaca, New York 14853, USA

[a)]Author to whom correspondence should be addressed: jac694@cornell.edu

ABSTRACT

$Sc_xAl_{1-x}N$ ($x = 0.18$–0.40) thin films of ∼28 nm thickness grown on metal polar GaN substrates by molecular beam epitaxy are found to exhibit smooth morphology with less than 0.5 nm roughness and predominantly single-phase wurtzite crystal structure throughout the composition range. Measurement of the piezoelectric d_{33} coefficient shows a 150% increase for lattice-matched $Sc_{0.18}Al_{0.82}N$ relative to pure aluminum nitride, whereas higher Sc contents exhibit lower piezoelectric coefficients. The electromechanical response of the epitaxial films correlates with the crystal quality and the presence of zinc blende inclusions, as observed by high-resolution electron microscopy. It is further found that the polarity of the epitaxial $Sc_xAl_{1-x}N$ layers is locked to the underlying substrate. The measured electromechanical properties of epitaxial $Sc_xAl_{1-x}N$, their relation to the atomic crystal structure and defects, and its crystal polarity provide useful guidance toward the applications of this material.

Published under license by AIP Publishing. https://doi.org/10.1063/5.0013943

Aluminum nitride (AlN) is a promising wide-bandgap, polar semiconductor with excellent electronic, optical, thermal, and mechanical properties.[1,2] Accordingly, AlN finds merit in numerous applications such as bulk and surface acoustic wave resonators,[3,4] RF transistor amplifiers,[5] ultraviolet light emitting diodes (LEDs),[6] and lasers.[7] To reach higher frequencies in RF filters for upcoming 5 G communications requires larger electromechanical coupling coefficients, which depend on the piezoelectric properties of the filter. Alloying AlN with scandium (Sc) in the wurtzite crystal structure has demonstrated many promising properties such as increased piezoelectric and pyroelectric coefficients and increased spontaneous polarization, and even ferroelectric behavior.[8–14] This is, in part, due to the large solubility of scandium in the wurtzite crystal structure and isoelectronic alloying as scandium adopts the +3 oxidation state when it substitutes the Al atom in AlN.[15–18]

Growth of epitaxial wurtzite $Sc_xAl_{1-x}N$ alloys is complex and presents several challenges to address, such as potential phase separation into nonpolar and non-piezoelectric rock salt scandium nitride (ScN), abnormal grain growth and microstructural instabilities, element and impurity segregation, and high oxygen incorporation.[19–28] Compared to the reported studies of the electromechanical properties and crystal structure of $Sc_xAl_{1-x}N$ deposited by sputtering-based techniques, those by the epitaxial methods of MBE and metalorganic chemical vapor deposition (MOCVD) are rare. MBE enables improvements to the crystalline, chemical, and electronic quality of $Sc_xAl_{1-x}N$ via deposition in an ultra-high vacuum environment on substrates of similar lattice symmetry. Recent reports of MBE growth have shown promising $Sc_xAl_{1-x}N$ crystalline quality with lower x-ray diffraction (XRD) rocking curve full-width-half-maximum (FWHM) values than by sputtering.[29–32] MBE grown $Sc_xAl_{1-x}N$ layers have shown promising electrical device performance[33–36] in high electron mobility transistors (HEMTs) and aim to build upon the technology advanced by sputtered films[37–44] by decreasing the thickness of the

Published under license by AIP Publishing

$Sc_xAl_{1-x}N$ active layers into the nanoscale regime, while still maintaining phase purity and structural integrity.

In this work, we report the structural and piezoelectric properties of epitaxial, single-crystalline $Sc_xAl_{1-x}N$ grown on low defect density bulk n type GaN substrates. $Sc_xAl_{1-x}N$ ($x = 0.18$) is observed to be lattice matched to GaN via reciprocal space mapping (RSM), exhibiting extremely high crystalline quality and a d_{33} piezoelectric coefficient of 15 pm/V. This is a 150% increase over the corresponding value measured in a pure AlN/GaN heterostructure control sample. *In situ* reflection high-energy electron diffraction (RHEED) images for $Sc_xAl_{1-x}N$ ($x = 0.18$, 0.25, 0.33, and 0.40) indicate epitaxial growth for all Sc compositions, with $x = 0.40$ being the highest Sc content reported to date on GaN. Atomic force microscopy (AFM) images indicate extremely smooth surface morphologies. Piezoresponse force microscopy (PFM), which is unstudied in MBE grown $Sc_xAl_{1-x}N$ to date, indicates an increase in the piezoelectric response relative to AlN. The highest piezoelectric enhancement is for the lattice-matched epitaxial $Sc_{0.18}Al_{0.82}N$, and a decrease past 18% Sc with increasing lattice mismatch and defect generation. This is corroborated with atomic resolution, aberration corrected STEM imaging that gives unique insight into structural defects in this material system. These defects include partial dislocations and zinc blende inclusions, which are detrimental to the piezoelectric response of the high-Sc content $Sc_xAl_{1-x}N$ layers.

The thin films were grown by MBE in a Veeco® GenXplor system with a base pressure of 10^{-10} Torr on Suzhou Nanonwin® 7 mm × 7 mm n-type GaN substrates. A Sc metal source of 99.9% purity (including C and O impurities) from Ames Laboratory was evaporated in a W crucible using a Telemark® electron beam evaporation system in the MBE environment. Flux stability was achieved with an Inficon® electron impact emission spectroscopy (EIES) system by directly measuring the Sc atomic optical emission spectra. Aluminum (99.9999% purity), gallium (99.99999% purity), and silicon (99.9999% purity) were supplied using Knudsen effusion cells. Nitrogen (99.99995%) active species were supplied using a Veeco® RF UNI-Bulb plasma source, with a growth pressure of approximately 10^{-5} Torr. The reported growth temperature is the heater temperature on the backside of the substrate measured by a thermocouple. *In situ* monitoring of film growth was performed using a KSA Instruments RHEED apparatus with a Staib electron gun operating at 15 kV and 1.5 A. Post-growth XRD was performed on a PanAlytical Empyrean diffractometer at 45 kV, 40 mA with Cu Kα1 radiation (1.54057 Å). Post-growth AFM and PFM measurements were performed using an Asylum Research Cipher ES system. PFM measurements were performed at contact resonance in a Dual AC Resonance Tracking (DART) mode. The underlying n-type GaN substrate was used as the bottom electrode and a conductive AFM tip [Nanosensors PointProbe Plus (PPP)-Electrostatic force microscopy (EFM)] was used as the top electrode. TEM cross-sectional samples were prepared via a focused ion beam (FIB) lift-out method using a Thermo Fisher Helios G4 UX FIB. Protective layers of platinum and carbon were sputtered prior to the FIB to prevent surface damage. High-angle annular dark field scanning transmission electron microscopy (HAADF-STEM) was performed using a convergence angle of 21 mrad in an aberration-corrected FEI Themis Titan microscope operating at 300 keV.

$Sc_xAl_{1-x}N$ thin films of ~30 nm thickness were deposited on the (0001) oriented Ga polar n^+GaN bulk substrates at a 200 W RF nitrogen plasma power and a 1.95 sccm flow rate. Sc and Al atomic percentages in the film were adjusted by the flux ratio of the evaporated Sc and Al species. A thin, ~5 nm layer of n^+ GaN ($N_D \sim 10^{19}/cm^3$ Si doping) was grown first before the epitaxy of the $Sc_xAl_{1-x}N$ layers to avoid nucleating directly on the substrate exposed to air. Excess Ga was desorbed with a growth interruption before the deposition of $Sc_xAl_{1-x}N$ to avoid chemical intermixing. Scandium and aluminum were co-deposited continuously during the growth of $Sc_xAl_{1-x}N$, and the respective shutters were closed simultaneously immediately after the layer growth. A nitrogen-rich condition (III/V ratio of ~0.85) was used to grow the $Sc_xAl_{1-x}N$ layers. This was done to avoid excess metal accumulation on the surface and prevent undesirable formation of Sc–Al containing intermetallic compounds in metal-rich conditions which are observed when the III/V ratio is greater than 1. To calibrate the active nitrogen flux (fraction of the total nitrogen species that contribute to growth) at 200 W and 1.95 sccm, control homoepitaxial growths of AlN on AlN/Al_2O_3 template substrates were conducted in advance. Monitoring the RHEED intensity of the 1 × 1 streaks of such growths sharply demarcates the required growth condition between metal-rich and nearly stoichiometric growth of AlN.

A summary of $Sc_xAl_{1-x}N$ samples grown in metal-rich and nitrogen-rich conditions, with varying Sc concentration and growth temperatures, is shown in Table I. Higher growth temperatures resulted in rough surface morphologies. As seen in the last four rows of Table I, a N-rich growth condition at a temperature of 600 °C is found to prevent the Al desorption and phase separation into ScN that occur at higher growth temperatures, since rock salt ScN is the thermodynamically stable phase at high Sc compositions.[31] If the substrate temperature is decreased significantly (e.g., 550 °C), RMS roughness significantly increases to 9.1 nm. If metal-rich growth conditions are used, the resulting films are significantly rougher. Overall, if growth conditions deviate from N-rich at ~600 °C, the surfaces were very rough even for very thin (~25 nm) layers.

For the optimal growth at 600 °C with a III/V ratio of 0.85, Fig. 1 shows the post-growth *in situ* RHEED patterns of the $x = 0.18$–0.40

TABLE I. Summary of $Sc_xAl_{1-x}N$ growth conditions and resulting film properties. N^* denotes active nitrogen: the concentration of nitrogen species in the plasma that contributes to growth. Nitrogen-rich growth conditions lead to much smoother samples with higher crystalline quality. The samples italicized are those mentioned in this report in further detail.

x	III/V ratio (Sc+Al/N*)	Substrate temp. (°C)	Film thickness (nm)	RMS roughness (nm)
0.18	1.15	650	25	2.1
0.18	1.15	600	25	1.3
0.18	1.15	550	25	9.1
0.10	1.15	750	30	3.1
0.15	1.15	750	30	3.0
0.27	1.15	750	30	2.5
0.45	1.15	750	30	11.9
0.18	*0.85*	*600*	*28*	*0.16*
0.25	*0.85*	*600*	*28*	*0.46*
0.33	*0.85*	*600*	*28*	*0.32*
0.40	*0.85*	*600*	*28*	*0.26*

Published under license by AIP Publishing

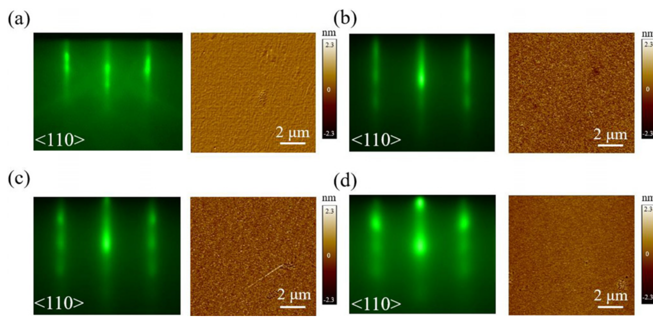

FIG. 1. RHEED images along the ⟨110⟩ zone axis for $Sc_xAl_{1-x}N$ x = 0.18 (a), x = 0.25 (b), x = 0.33% (c), and x = 0.40 (d). Corresponding 10 × 10 μm AFM images, indicating epitaxial growth, no evidence of secondary phases and smooth surface morphologies.

$Sc_xAl_{1-x}N$ layers, viewed along the $\langle 11\bar{2}0\rangle$ azimuth, with the corresponding measured ex-situ surface morphologies. For $Sc_xAl_{1-x}N$ (x = 0.18), Kikuchi lines intersecting the 1 × 1 streak patterns are seen [Fig. 1(a)], indicating a high crystalline quality and coherence. This is in accordance with $Sc_xAl_{1-x}N$ (x = 0.18) being lattice matched to the in-plane lattice parameter of GaN.[45] As the Sc content is increased further, the lattice mismatch with GaN increases and the RHEED patterns become increasingly spotty and diffuse, indicative of decreasing crystalline quality. Though, as the Sc content is increased, the wurtzite crystal structure becomes less thermodynamically stable, no additional diffraction spots or rotation of diffraction features are seen. This suggests that no additional phases other than the wurtzite phase are formed during the growth of all $Sc_xAl_{1-x}N$ compositions studied here. The corresponding AFM images in Fig. 1 indicate that the root-mean squared (RMS) surface roughness of the as-grown layers is 0.16, 0.46, 0.32, and 0.26 nm for $Sc_xAl_{1-x}N$ (x = 0.18, 0.25, 0.33, and 0.40), respectively. Thus, extremely smooth $Sc_xAl_{1-x}N$ layers result from the epitaxial, phase pure MBE growth.

Figure 2(a) shows the symmetric 2Θ-ω XRD scans, indicating wurtzite $Sc_xAl_{1-x}N$ 0002 diffraction peaks near 36 and 37° 2Θ. As the Sc content is increased (x > 0.18), the 0002 diffraction peak shifts to higher 2Θ values, indicating a decrease in the out-of-plane c-lattice parameter as the Sc content is increased. The measured out-of-plane lattice parameters from the 2Θ-ω scans are 4.99, 4.98, 4.90, and 4.89 Å for x = 0.18, x = 0.25, x = 0.33, and x = 0.40, respectively, consistent with a decreasing c/a ratio relative to AlN with an increasing Sc content.[32] The rocking curve FWHM for $Sc_xAl_{1-x}N$ (x = 0.18, 0.25, and 0.33) 0002 diffraction peaks (not shown) are 0.09, 0.11, and 0.12°, respectively. These values are indicative of a high crystalline quality for the thin (~28 nm) epitaxial layers. Figure 2(b) shows the grazing exit, asymmetric RSM mapping of the (11–24) $Sc_xAl_{1-x}N$ peak for the x = 0.18 sample. It indicates coherent strain, as the in-plane reciprocal lattice unit Q_x is the same for the substrate and the film. From the respective Q_x and Q_y values, the lattice parameters obtained for $Sc_xAl_{1-x}N$ (x = 0.18) are 3.18 Å in-plane and 4.99 Å out-of plane, consistent with a prior report.[45]

The piezoelectric properties of the epitaxial $Sc_xAl_{1-x}N$ layers were then measured. For calibration, and to set a baseline value for 0% Sc, an AlN layer of ~5 nm was grown on an identical n^+ GaN bulk substrate at 750 °C under metal-rich growth conditions. The 5 nm thickness prevents cracking of the AlN epilayer due to the in-plane biaxial tensile stress with the underlying GaN.[46] PFM measurements were performed to measure the piezoelectric coefficient $d_{33,eff}$. Combined AC and DC biases were applied to the bare surface to track contact resonance frequency and to bias the sample, respectively. Simultaneous topography and piezoresponse channels were detected during the measurement, with $d_{33,eff}$ values calculated by dividing the measured vertical displacement of the cantilever by the contact frequency resonance factor (Q) and the DC drive voltage. Because the RMS surface roughness for all epilayers was less than 0.5 nm, there were no additional errors that stemmed from rough surface morphologies.

Figures 3(a)–3(e) shows the surface PFM maps for the five samples. The piezoelectric coefficients shown in Fig. 3(f) are obtained from the slope of the measured displacement vs applied DC voltage (not shown). The value of $d_{33,eff}$ ~ 6 pm/V obtained for AlN is consistent with its known value, serving as a dependable calibration. For x = 0.18, a value of $d_{33,eff}$ ~ 15 pm/V is measured. This value is larger than the prior reported values of approximately 7, 8, and 14 pm/V[14,24–26,47,48] for compositions near 18% Sc. It is noted that

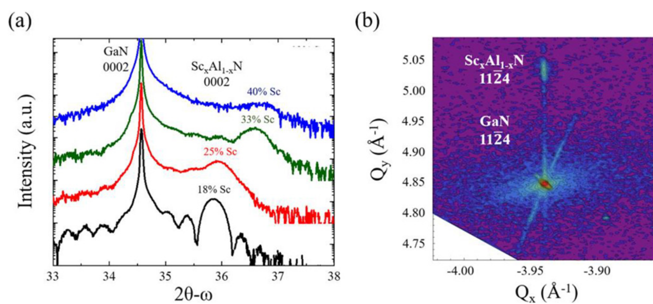

FIG. 2. (a) Symmetric 2Θ-ω XRD scans, showing $Sc_xAl_{1-x}N$ wurtzite 0002 peaks. Compared to the GaN 0002 peak, the $Sc_xAl_{1-x}N$ peak positions shift to higher 2Θ values as the Sc content increases, indicating a decrease in the out-of-plane lattice parameter. (b) Asymmetric RSM centered around the GaN 11–24 reflection for the x = 0.18 sample, indicating lattice-matching of $Sc_xAl_{1-x}N$ to the in-plane lattice parameter of GaN.

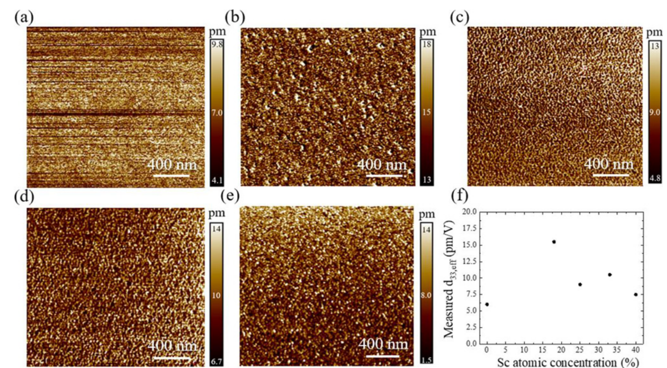

FIG. 3. Surface mapping of measured $d_{33,eff}$ coefficients via vertical PFM for (a) AlN, (b) $Sc_xAl_{1-x}N$ (x = 0.18), (c) $Sc_xAl_{1-x}N$ (x = 0.25), (d) $Sc_xAl_{1-x}N$ (x = 0.33), and (e) $Sc_xAl_{1-x}N$ (x = 0.40), showing relatively uniform $d_{33,eff}$ values across the surface. (f) Compiled graph of the piezoelectric coefficients $d_{33,eff}$ vs Sc concentration from PFM measurements shown in comparison to AlN, the control sample.

Published under license by AIP Publishing

most of the prior measurements did not utilize PFM and all were conducted on thicker, sputter deposited samples. The measured value of 15 pm/V represents a 150% enhancement in the piezoelectric coefficient for high-quality, lattice-matched $Sc_xAl_{1-x}N$ on GaN. This could be, in part, due to contribution from piezoelectric strain from the substrate and enhanced crystal quality, but the precise mechanism needs further investigation.

As the Sc content is increased further ($x > 0.18$), the measured values of $d_{33,eff}$ *decrease* to the range of 7–10 pm/V. The decrease in $d_{33,eff}$ observed here is attributed to the thinness of the layers, a polar substrate, and a decrease in the crystalline quality of the samples relative to $x = 0.18$, as is discussed next using electron microscopy. The trend is opposite to the trends in some reports on sputtered $Sc_xAl_{1-x}N$ samples of much greater thicknesses (greater than 250 nm), deposited on metallic and Si (100) substrates.[13,14,24,26] However, trends similar to those seen here have also been reported, where the measured piezoelectric coefficients depend on the crystalline and microstructural quality, which is affected by changes in deposition parameters and annealing treatments.[22–24,47,49–52] Surface mapping of the d_{33} values in Fig. 3 shows relatively uniform and consistent values over 2×2 μm image scans, as expected for epitaxial $Sc_xAl_{1-x}N$ layers with smooth surface morphologies.

To assess the structural quality of the $Sc_xAl_{1-x}N$ layers, the electron microscope images were taken of the lattice-matched $x = 0.18$ and the heavily mismatched $x = 0.40$ samples shown in Figs. 4(a) and 4(b). To determine the film quality, lines were drawn along the lattice planes over a large field of view HAADF-STEM images. The "T" marks the occurrence of an extra lattice plane, and, therefore, it can be counted as one dislocation occurring at that region (Larger versions in supplementary material Fig. 2). Comparison of (a) and (b) shows that $Sc_xAl_{1-x}N$ ($x = 0.18$) has a lower defect density and, therefore, higher film quality than $Sc_xAl_{1-x}N$ ($x = 0.40$). Annular bright field (ABF-STEM) image in c) shows both Sc/Al and N sublattices where we can determine the crystal structure to be wurtzite at the $Sc_xAl_{1-x}N$/GaN interface. The epitaxial $Sc_xAl_{1-x}N$ layer on GaN is seen to be metal polar, adopting the same polarity as the underlying GaN substrate.

Figure 5(a) shows the boxed area in Fig. 4(a), enlarged to show that the dislocation is due to an I_1-type stacking fault associated with an extra basal plane,[53] where a lattice stacking sequence of ABACA is identified on the right-hand-side of a partial dislocation, compared to the wurtzite ABAB stacking sequence on the left-hand-side. Figures 5(b) and 5(c) show a region with a cubic zinc blende structure near the top of the $Sc_xAl_{1-x}N$ ($x = 0.40$) film. Similar behavior has also been reported in epitaxial $Sc_xGa_{1-x}N$ thin films.[54] Overall, the zinc blende phase is not a thermodynamically stable phase at these Sc contents and, thus, may arise from kinetic factors during the growth process.

In conclusion, insight into the structural and piezoelectric properties of epitaxially grown $Sc_xAl_{1-x}N$ on GaN is achieved. Epitaxial, smooth films achieved using nitrogen-rich growth conditions reveal a ~150% enhancement of the piezoelectric coefficient of lattice-matched $Sc_{0.18}Al_{0.82}N$ relative to AlN. Atomic resolution STEM imaging shows partial dislocations arising from stacking faults in higher Sc content lattice-mismatched $Sc_xAl_{1-x}N$ and the presence of zinc blende inclusions, which reduce the measured piezoelectric coefficient. The polarity of the epitaxial $Sc_xAl_{1-x}N$ is found to be the same as the

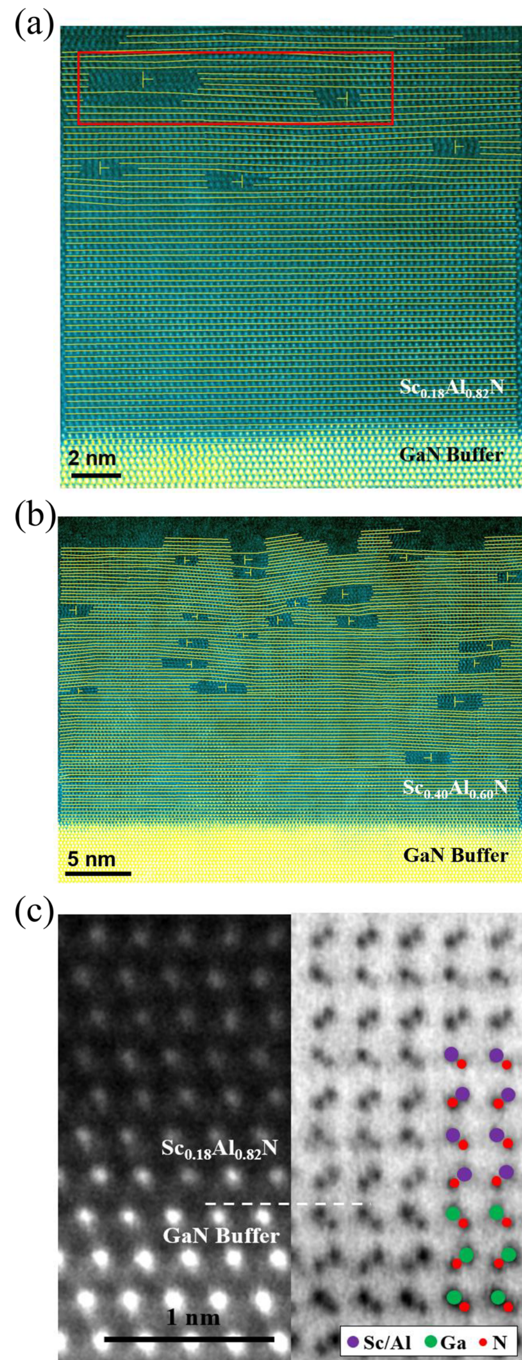

FIG. 4. STEM images of defects in $Sc_xAl_{1-x}N$ films ($x = 0.18$, 0.40). HAADF-STEM images showing an overview of (a) $Sc_{0.18}Al_{0.82}N$ and (b) $Sc_{0.40}Al_{0.60}N$ films that are overlaid with yellow lines drawn along each lattice plane perpendicular to the growth direction. The "T" marks the occurrence of an extra lattice plane. (b) shows a much higher stacking fault density compared to (a). ABF-STEM image in (c) shows an abrupt $Sc_{0.18}Al_{0.82}N$/GaN interface, where the metal polar orientation can be determined by the overlaid crystal structure. Sc/Al, Ga, and N correspond to purple, green, and red atoms, respectively.

Published under license by AIP Publishing

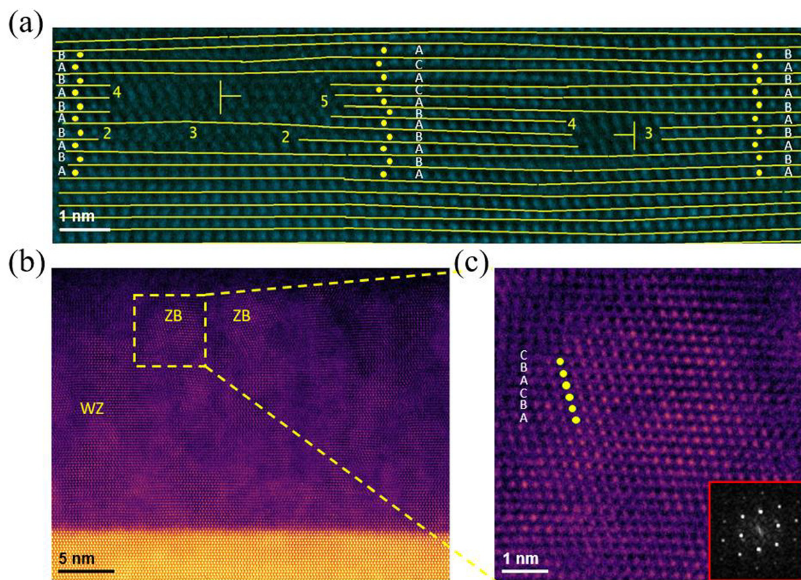

FIG. 5. Stacking faults in $Sc_xAl_{1-x}N$ films (x = 0.18, 0.40). (a) Magnified region in the $Sc_{0.18}Al_{0.82}N$ film from the red box in Fig. 4(a), where the *AB* stacking of the wurtzite structure is labeled on the left. *ABCB* stacking is identified on the right; therefore, a fault can be identified at the center of these two stacking sequences. The numbers denoted on either side of the stacking fault indicate the number of planes, showing that the defects are partial dislocations associated with a stacking fault. (b) Low magnification image of the $Sc_{0.40}Al_{0.60}N$ film of mainly wurtzite structure having zinc blende inclusions toward the surface of the film. (c) Magnified image from the yellow box from (b), showing the *ABC* stacking of the lattice. The diffractogram of the image shown as the inset confirms the zinc blende structure.

underlying GaN substrate. Future work will need to further evaluate the piezoelectric coefficients of thicker $Sc_xAl_{1-x}N$ films and heterostructures grown on metallic electrodes. In addition, further study of the effects of growth conditions and post-growth annealing of the $Sc_xAl_{1-x}N$ films can reveal if the defects such as stacking faults and cubic inclusions can be prevented or reduced in the epitaxial films. This will enable the optimal structural and piezoelectric performance of epitaxial $Sc_xAl_{1-x}N$/GaN heterostructures.

See the supplementary material for further details and data regarding the STEM measurements of $Sc_xAl_{1-x}N$.

This work was supported by the DARPA Tunable Ferroelectric Nitrides (TUFEN) program monitored by Dr. Ronald G. Polcawich. The work was also supported, in part, by Cornell's nanoscale facility (Grant No. NCCI-1542081), AFOSR Grant Nos. FA9550-20-1-0148 and NSF DMR-1710298, National Science Foundation Award/Contract No. NSF-MRI-1631282, and the Cornell Center for Materials Research Shared Facilities, which are supported through the NSF MRSEC program (No. DMR-1719875). This work made use of a Helios FIB supported by NSF (No. DMR-1539918) and an FEI Titan Themis 300, which was acquired through No. NSF-MRI-1429155, with additional support from Cornell University, the Weill Institute, and the Kavli Institute at Cornell. The authors would also like to acknowledge Matt Besser and the Materials Preparation Center at Ames Laboratory for supplying the Sc source material.

DATA AVAILABILITY

The data that support the findings of this study are available from the corresponding author upon reasonable request.

REFERENCES

[1]L. E. McNeil, M. Grimsditch, and R. H. French, J. Am. Ceram. Soc. **76**, 1132 (1993).
[2]R. L. Xu, M. Muñoz Rojo, S. M. Islam, A. Sood, B. Vareskic, A. Katre, N. Mingo, K. E. Goodson, H. G. Xing, D. Jena, and E. Pop, J. Appl. Phys. **126**, 185105 (2019).
[3]M.-A. Dubois, P. Muralt, and V. Plessky, in *IEEE International Ultrasonics Symposium* (IEEE, Caesars Tahoe, NV, USA, 1999), pp. 907–910.
[4]M. D. Hodge, R. Vetury, S. R. Gibb, M. Winters, P. Patel, M. A. McLain, Y. Shen, D. H. Kim, J. Jech, K. Fallon, R. Houlden, D. M. Aichele, and J. B. Shealy, in *IEEE International Electron Devices Meeting (IEDM)* (IEEE, San Francisco, CA, USA, 2017), pp. 25.6.1–25.6.4.
[5]A. Hickman, R. Chaudhuri, S. J. Bader, K. Nomoto, K. Lee, H. G. Xing, and D. Jena, IEEE Electron Device Lett. **40**, 1293 (2019).
[6]S. M. Islam, K. Lee, J. Verma, V. Protasenko, S. Rouvimov, S. Bharadwaj, H. (Grace) Xing, and D. Jena, Appl. Phys. Lett. **110**, 041108 (2017).
[7]Z. Zhang, M. Kushimoto, T. Sakai, N. Sugiyama, L. J. Schowalter, C. Sasaoka, and H. Amano, Appl. Phys. Express **12**, 124003 (2019).
[8]S. Fichtner, N. Wolff, F. Lofink, L. Kienle, and B. Wagner, J. Appl. Phys. **125**, 114103 (2019).
[9]S. Bette, S. Fichtner, S. Bröker, L. Nielen, T. Schmitz-Kempen, B. Wagner, C. Van Buggenhout, S. Tiedke, and S. Tappertzhofen, Thin Solid Films **692**, 137623 (2019).
[10]N. Kurz, Y. Lu, L. Kirste, M. Reusch, A. Žukauskaitė, V. Lebedev, and O. Ambacher, Phys. Status Solidi A **215**, 1700831 (2018).
[11]M. A. Caro, S. Zhang, T. Riekkinen, M. Ylilammi, M. A. Moram, O. Lopez-Acevedo, J. Molarius, and T. Laurila, J. Phys.: Condens. Matter **27**, 245901 (2015).
[12]M. Akiyama, T. Kamohara, K. Kano, A. Teshigahara, Y. Takeuchi, and N. Kawahara, Adv. Mater. **21**, 593 (2009).
[13]M. Akiyama, K. Kano, and A. Teshigahara, Appl. Phys. Lett. **95**, 162107 (2009).
[14]Y. Lu, M. Reusch, N. Kurz, A. Ding, T. Christoph, M. Prescher, L. Kirste, O. Ambacher, and A. Žukauskaitė, APL Mater. **6**, 076105 (2018).
[15]K. R. Talley, S. L. Millican, J. Mangum, S. Siol, C. B. Musgrave, B. Gorman, A. M. Holder, A. Zakutayev, and G. L. Brennecka, Phys. Rev. Mater. **2**, 063802 (2018).
[16]M. A. Moram and S. Zhang, J. Mater. Chem. A **2**, 6042 (2014).
[17]S. Zhang, D. Holec, W. Y. Fu, C. J. Humphreys, and M. A. Moram, J. Appl. Phys. **114**, 133510 (2013).
[18]D. Jena, R. Page, J. Casamento, P. Dang, J. Singhal, Z. Zhang, J. Wright, G. Khalsa, Y. Cho, and H. G. Xing, Jpn. J. Appl. Phys., Part 1 **58**, SC0801 (2019).
[19]J. Casamento, H. G. Xing, and D. Jena, Phys. Status Solidi B **257**, 1900612 (2020).
[20]M. Li, J. Xie, B. Chen, N. Wang, and Y. Zhu, in *IEEE International Ultrasonics Symposium (IUS)* (IEEE, Glasgow, United Kingdom, 2019), pp. 1124–1126.

Published under license by AIP Publishing

[21]C. S. Sandu, F. Parsapour, S. Mertin, V. Pashchenko, R. Matloub, T. LaGrange, B. Heinz, and P. Muralt, Phys. Status Solidi A **216**, 1800569 (2019).
[22]Y. Lu, M. Reusch, N. Kurz, A. Ding, T. Christoph, L. Kirste, V. Lebedev, and A. Žukauskaitė, Phys. Status Solidi A **215**, 1700559 (2018).
[23]P. M. Mayrhofer, P. O. Å. Persson, A. Bittner, and U. Schmid, Microsyst. Technol. **22**, 1679 (2016).
[24]A. Zukauskaite, G. Wingqvist, J. Palisaitis, J. Jensen, P. O. Å. Persson, R. Matloub, P. Muralt, Y. Kim, J. Birch, and L. Hultman, J. Appl. Phys. **111**, 093527 (2012).
[25]F. Parsapour, V. Pashchenko, S. Mertin, C. Sandu, N. Kurz, P. Nicolay, and P. Muralt, in *IEEE International Ultrasonics Symposium (IUS)* (IEEE, Washington, DC, USA, 2017), pp. 1–4.
[26]S. Mertin, V. Pashchenko, F. Parsapour, C. Nyffeler, C. S. Sandu, B. Heinz, O. Rattunde, G. Christmann, M.-A. Dubois, and P. Muralt, in *IEEE International Ultrasonics Symposium (IUS)* (IEEE, Washington, DC, USA, 2017), pp. 1–4.
[27]O. Zywitzki, T. Modes, S. Barth, H. Bartzsch, and P. Frach, Surf. Coat. Technol. **309**, 417 (2017).
[28]D. Wu, Y. Chen, S. Manna, K. Talley, A. Zakutayev, G. L. Brennecka, C. V. Ciobanu, P. Constantine, and C. E. Packard, IEEE Trans. Ultrason., Ferroelectr., Freq. Control **65**, 2167 (2018).
[29]P. Wang, D. A. Laleyan, A. Pandey, Y. Sun, and Z. Mi, Appl. Phys. Lett. **116**, 151903 (2020).
[30]K. Frei, R. Trejo-Hernández, S. Schütt, L. Kirste, M. Prescher, R. Aidam, S. Müller, P. Waltereit, O. Ambacher, and M. Fiederle, Jpn. J. Appl. Phys., Part 1 **58**, SC1045 (2019).
[31]M. T. Hardy, B. P. Downey, N. Nepal, D. F. Storm, D. S. Katzer, and D. J. Meyer, Appl. Phys. Lett. **110**, 162104 (2017).
[32]R. Dargis, A. Clark, A. Ansari, Z. Hao, M. Park, D. Kim, R. Yanka, R. Hammond, M. Debnath, and R. Pelzel, Phys. Status Solidi A **217**, 1900813 (2020).
[33]T. E. Kazior, E. M. Chumbes, B. Schultz, J. Logan, D. J. Meyer, and M. T. Hardy, in *IEEE MTT-S International Microwave Symposium (IMS)* (IEEE, Boston, MA, USA, 2019), pp. 1136–1139.
[34]A. J. Green, J. K. Gillespie, R. C. Fitch, D. E. Walker, M. Lindquist, A. Crespo, D. Brooks, E. Beam, A. Xie, V. Kumar, J. Jimenez, C. Lee, Y. Cao, K. D. Chabak, and G. H. Jessen, IEEE Electron Device Lett. **40**, 1056 (2019).
[35]M. Park, Z. Hao, D. G. Kim, A. Clark, R. Dargis, and A. Ansari, in *20th International Conference on Solid-State Sensors and Actuators Microsystems & Eurosensors XXXIII (TRANSDUCERS & EUROSENSORS XXXIII)* (IEEE, Berlin, Germany, 2019), pp. 450–453.
[36]A. Ansari, in *IEEE MTT-S International Wireless Symposium (IWS)* (IEEE, Guangzhou, China, 2019), pp. 1–3.
[37]Q. Wang, Y. Lu, S. Mishin, Y. Oshmyansky, and D. A. Horsley, J. Microelectromech. Syst. **26**, 1132 (2017).
[38]P. M. Mayrhofer, E. Wistrela, M. Kucera, A. Bittner, and U. Schmid, in *Transducers—18th International Conference on Solid-State Sensors Actuators and Microsystems (TRANSDUCERS)* (IEEE, Anchorage, AK, USA, 2015), pp. 2144–2147.
[39]M. Dorfmeister, M. Schneider, and U. Schmid, in *20th International Conference on Solid-State Sensors, Actuators and Microsystems and Eurosensors XXXIII (TRANSDUCERS & EUROSENSORS XXXIII)* (IEEE, Berlin, Germany, 2019), pp. 853–856.
[40]P. M. Mayrhofer, C. Rehlendt, M. Fischeneder, M. Kucera, E. Wistrela, A. Bittner, and U. Schmid, J. Microelectromech. Syst. **26**, 102 (2017).
[41]Y. Kusano, I. Ishii, T. Kamiya, A. Teshigahara, G.-L. Luo, and D. A. Horsley, IEEE Trans. Ultrason., Ferroelectr., Freq. Control **66**, 1488 (2019).
[42]S. Rassay, F. Hakim, M. Ramezani, and R. Tabrizian, in *IEEE 33rd International Conference Micro Electro Mechchanical Systems (MEMS)* (IEEE, Vancouver, BC, Canada, 2020), pp. 1254–1257.
[43]B. P. Sorokin, A. S. Novoselov, G. M. Kvashnin, N. V. Luparev, N. O. Asafiev, A. B. Shipilov, and V. V. Aksenenkov, Acoust. Phys. **65**, 263 (2019).
[44]V. Pashchenko, R. Matloub, F. Parsapourkolour, P. Muralt, S. Ballandras, and K. Haffner, in *IEEE International Ultrasonics Symposium (IUS)* (IEEE, Tours, 2016), pp. 1–4.
[45]S. Leone, J. Ligl, C. Manz, L. Kirste, T. Fuchs, H. Menner, M. Prescher, J. Wiegert, A. Žukauskaitė, R. Quay, and O. Ambacher, Phys. Status Solidi RRL **14**, 1900535 (2020).
[46]Y. Cao and D. Jena, Appl. Phys. Lett. **90**, 182112 (2007).
[47]J. Tang, D. Niu, Z. Tai, and X. Hu, J. Mater. Sci. **28**, 5512 (2017).
[48]A. Žukauskaitė, E. Broitman, P. Sandström, L. Hultman, and J. Birch, Phys. Status Solidi A **212**, 666 (2015).
[49]J. Yang, X. Meng, C. Yang, and Y. Zhang, Appl. Surf. Sci. **287**, 355 (2013).
[50]M. Akiyama, T. Tabaru, K. Nishikubo, A. Teshigahara, and K. Kano, J. Ceram. Soc. Jpn. **118**, 1166 (2010).
[51]C. S. Sandu, F. Parsapour, D. Xiao, R. Nigon, L. M. Riemer, T. LaGrange, and P. Muralt, Thin Solid Films **697**, 137819 (2020).
[52]T. Tabaru and M. Akiyama, Thin Solid Films **692**, 137625 (2019).
[53]V. Potin, P. Ruterana, and G. Nouet, J. Phys.: Condens. Matter **12**, 10301 (2000).
[54]S. M. Knoll, S. K. Rhode, S. Zhang, T. B. Joyce, and M. A. Moram, Appl. Phys. Lett. **104**, 101906 (2014).

Published under license by AIP Publishing